SUPPLEMENTARY INFORMATION

Long-range transport of 2D excitons in dynamic acoustic lattice

Ruoming Peng[1], Adina Ripin[2], Yusen Ye[3], Jiayi Zhu[2], Changming Wu[1], Seokhyeong Lee[1], Huan Li[1,*], K. Watanabe[4], T. Taniguchi[4], Ting Cao[3], Xiaodong Xu[2,3], Mo Li[1,2,†]

[1]*Department of Electrical and Computer Engineering, University of Washington, Seattle, WA 98195, USA*

[2]*Department of Physics, University of Washington, Seattle, WA 98195, USA*

[3]*Department of Material Science and Engineering, University of Washington, Seattle, WA 98195, USA*

[4]*Research Center for Functional Materials, National Institute for Materials Science, Tsukuba, Japan*

1. Theory of exciton transport driven by surface acoustic waves

In the IXs of bilayer WSe_2, the bound electrons and holes live, respectively, in the Q (also called Λ in literature) and the K valleys of the Brillouin zone[1–3]. Due to the spin-valley locking of bilayer WSe_2, the dipole moment of an IX can point along the +z or -z directions, depending on the layer localization of the electron and the hole in the IX. Under the periodic out-of-plane electric field induced by the SAW, the two types of IXs with opposite dipoles are driven to two nearby field extrema separated by half acoustic wavelength and propagate together in the same direction.

In the temperature range of 6 K – 300 K, excitons have average kinetic energy of 0.6 meV – 26 meV. Taking the effective mass of an exciton to be ~ m_e (bare electron mass), the thermal velocity v_{IX} of the exciton is in the range of 1.5×10^4 – 9.6×10^4 m/s. This value is an order of magnitude lager than the travelling velocity of SAW (~3.5×10^3 m/s). As a result, the IX ensemble can be approximated as an exciton gas under quasi-equilibrium, when it is trapped at the minima of the slowly-varying potential energy landscape. Here the trap can arise either from disorder or from the electric field gradient induced by SAW.

We next model the transport of excitons in the realistic bilayer WSe_2 device, assuming that the excitons do not recombine during the transport. The surface potential disorder caused by strain and other imperfections are described by potential wells that can trap excitons (Fig. SI-1 a), with a characteristic barrier height of Δ and length L. If L is much smaller than the wavelength of the SAW, the electric field gradient of SAW can help the excitons to overcome these potential barriers. An exciton that is not localized by the disorder should have kinetic energy larger than $E_{\min} = \Delta - (\nabla E_{z-\max} \bullet \mathbf{p}) L$ (Fig. SI-1 b) to overcome the barrier, where ∇E_{z-max} refers to the maximum gradient of the electric field induced by the SAW. Under quasi-equilibrium, the population n of these excitons:

* Present Address: Zhejiang University, China

† Email: moli96@uw.edu

$$n(\nabla E_{z-\max}, T) \sim \int_{E_{\min}}^{\infty} dE\, e^{-\frac{E-\mu}{k_B T}} \sim e^{\frac{L p}{k_B T}\nabla E_{z-\max}}$$

The density of states factor is taken as a step function for 2D excitons.

At 100K, the PL intensity at the edge of the bilayer WSe_2 flake should be proportional to n. As the maximum electric field gradient induced by SAW is proportional to the square root of SAW power $\nabla E_{z-max} \sim \sqrt{P_s}$, we fit the PL intensity with $n(P_s) = n_0 e^{\sqrt{P_s/P_t}}$, where P_t is a temperature and sample-quality dependent factor, above which the exciton can respond efficiently to the electric field generated by SAW. Fig. SI-1 c shows this exponential dependence is consistent with experimental observations.

Supplementary Figure 1. Exciton transport by surface acoustic wave under disorder potential. (a) Schematic exciton gas in a trap with a characteristic depth in energy of Δ and length L. The exciton gas in quasi-equilibrium is shown in orange. (b) Schematic exciton gas when maximum electric potential gradient from SAW is applied, creating a shallower potential barrier on one side of the trap. The exciton population above the dotted line can travel with SAW. (c) Fitting the power-dependent PL intensity to the SAW power.

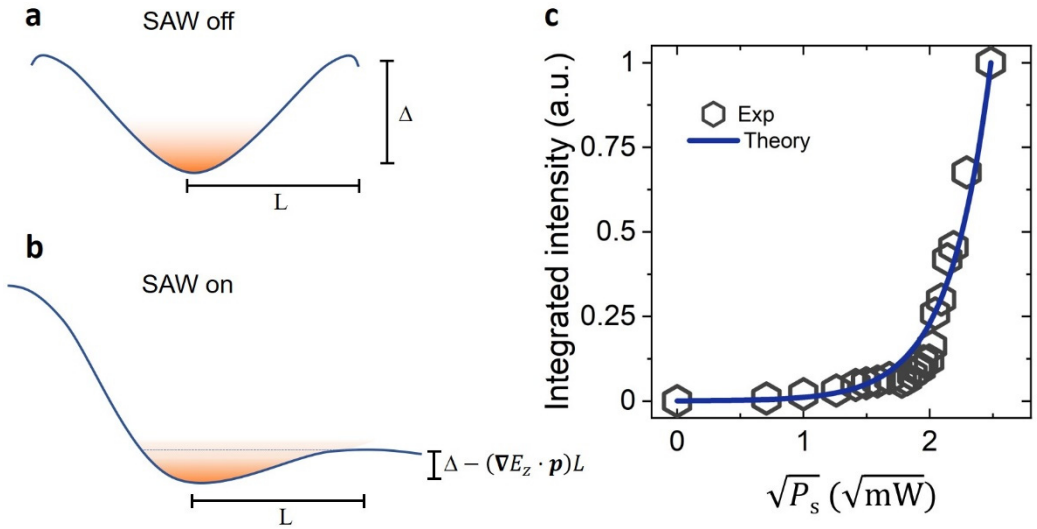

2. Measurement Setup

A continuous-wave He-Ne laser (633 nm) was used to excite the excitons in bilayer WSe_2. With an objective lens (NA=0.42), the laser beam was focused with a diffraction-limited spot size of about 1 μm. The sample was mounted in a cryostat (Montana Instrument) with an optical window for optical access. Meanwhile, the RF signal was generated by a vector network analyzer (VNA)

(Agilent E8362B) and then coupled to the wire-bonded device inside the cryostat. The calibration kits (Keysight 8052D) were used to de-embed the system so that the IDT resonance can be resolved. The interlayer exciton emission was acquired with a spectrometer (Princeton Instrument) after the laser line was removed with a 633 notch filter (Thorlabs). To image the spatial transport of the exciton, the center wavelength of the spectrometer was set to be 0 so it functioned like a mirror. The filtered signal was then collected by a cooled camera (Pixis 400) operating at -70 °C to improve the signal-to-noise ratio. To collect the spectrum results, we set the center wavelength to 790 nm, which covered the emission spectrum of the interlayer exciton. To perform the spectral-PL imaging measurement of the exciton transport, the transport direction was aligned with the slit of the spectrometer, while the x-axis of the CCD camera displayed the spectrum information. The y-axis signal gave the spatial emission of the bilayer devices.

3. Device fabrication

The WSe_2 device was fabricated by the standard polymer-assisted (PC) pick-up method[4,5]. The 2D flakes of hBN and WSe_2 (HQ graphene) were exfoliated to a 90 nm SiO_2/ Si substrate and then picked up using PC/PDMS (Sylgard 184) stamps. The bilayer WSe_2 flakes were identified by their optical contrast and then confirmed with photoluminescent measurements. The IDTs were patterned on a y-cut $LiNbO_3$ wafer (MTI) using ebeam lithography. The IDT is aligned to generate SAW propagating along the z-axis of the $LiNbO_3$ wafer. Layers of 12 nm chromium and 120 nm gold were deposited using an ebeam evaporator under high vacuum. Aligned transfer was then done by a home-built transfer stage with high accuracy so that the WSe_2/hBN heterostructure was precisely aligned at the focus region of the curved IDTs. PC residue was then removed using chloroform for 1 h and followed by a 5 min rinsing in the IPA. Finally, aligned ebeam writing was performed and 50 nm indium-tin-oxide (ITO) was deposited by a sputtering system (Evatec LLS EVO) under O_2 condition. After deposition, the device was annealed in atmosphere at 300 °C for 5 min to improve the conductivity of the ITO film, which can ensure a better screening of the in-plane field.

Supplementary Figure 2. Emission spectrum at the pump position when T=6 K. When the SAW is on, all the sharp emission resonances disappear due to delocalization of the excitons and reduced coupling with localized phonon modes.

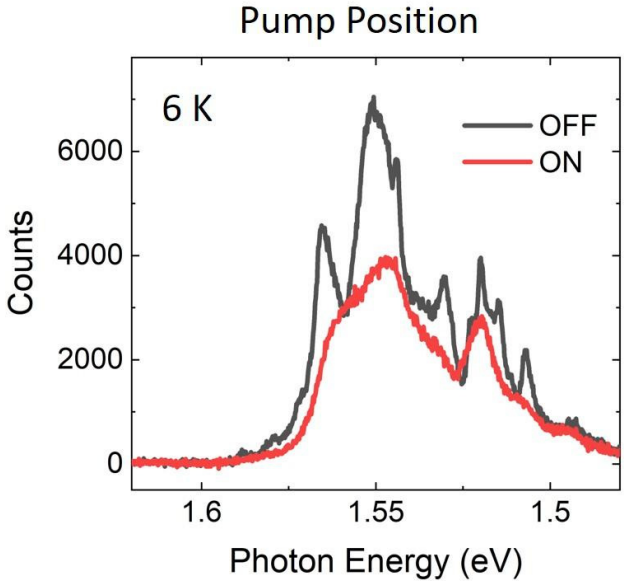

Supplementary Figure 3. The emission spectrum at the pump (a) and edge (b) position when T=30 K.

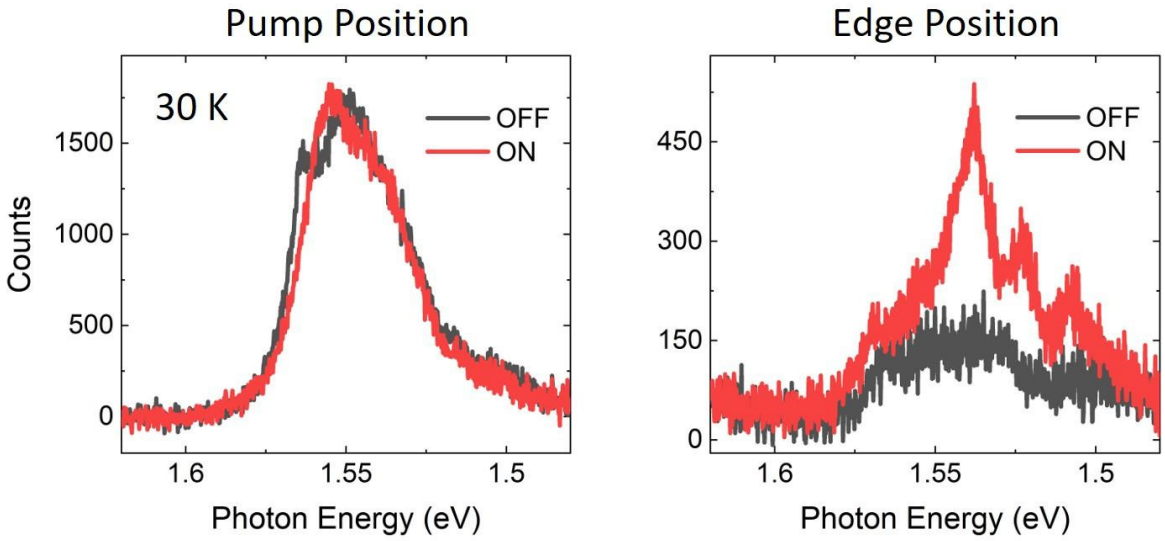

Supplementary Figure 4. The emission spectrum at the pump (a) and edge (b) position when T=200 K.

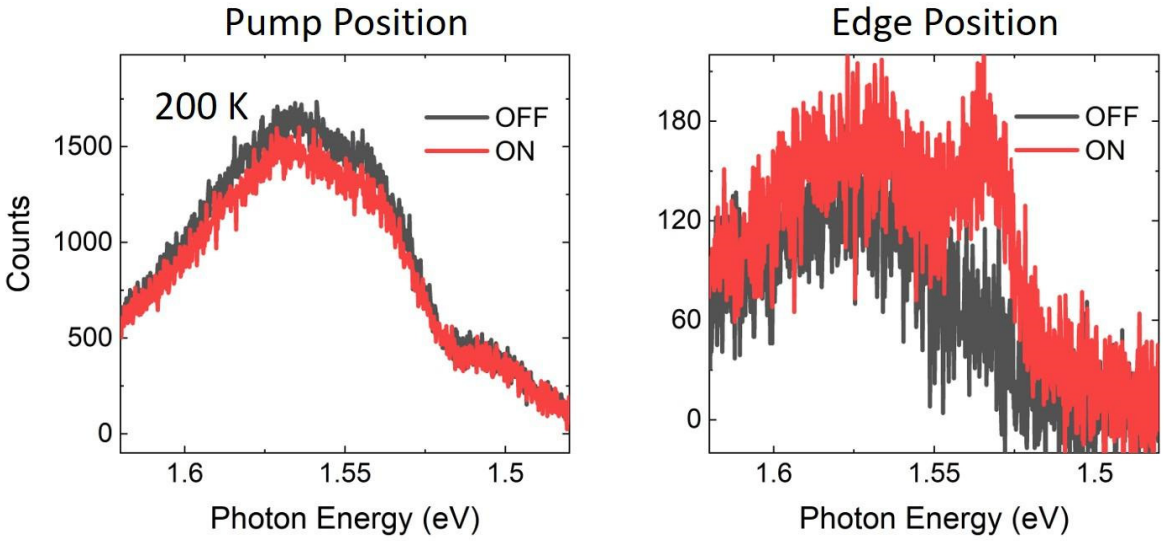

Supplementary Figure 5. Exciton transport at 50 K.

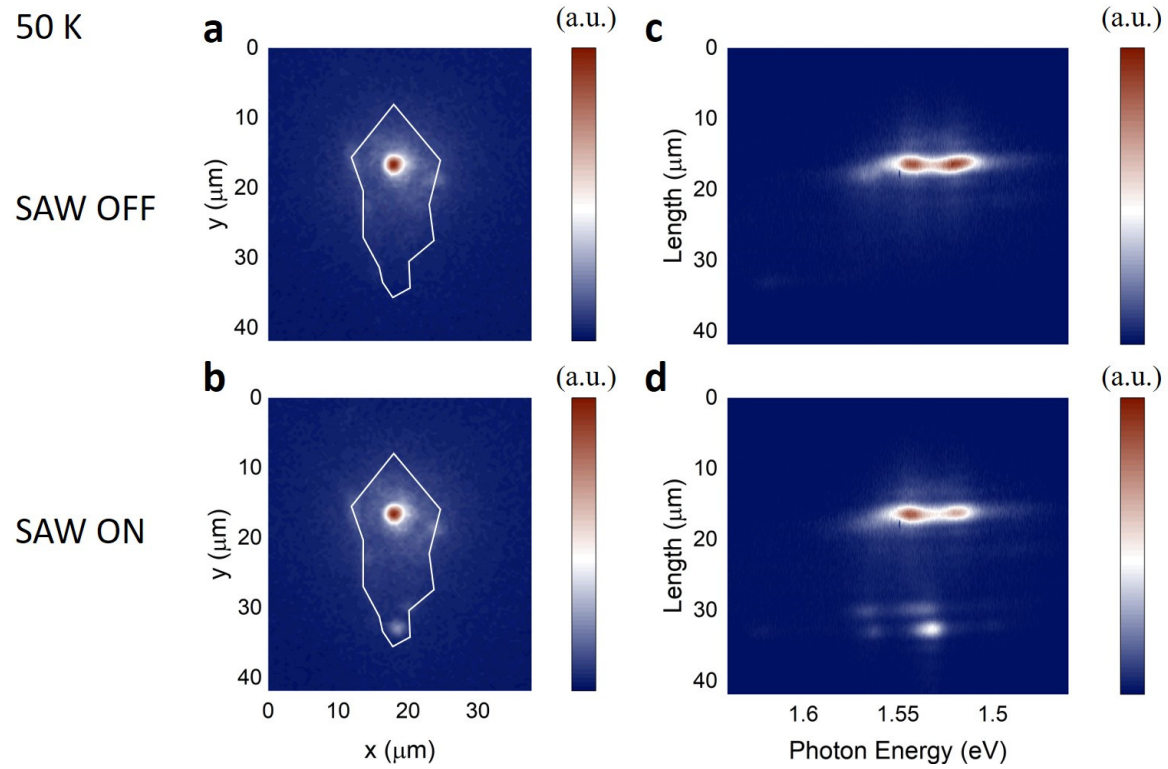

Supplementary Figure 6. Exciton transport at 80 K.

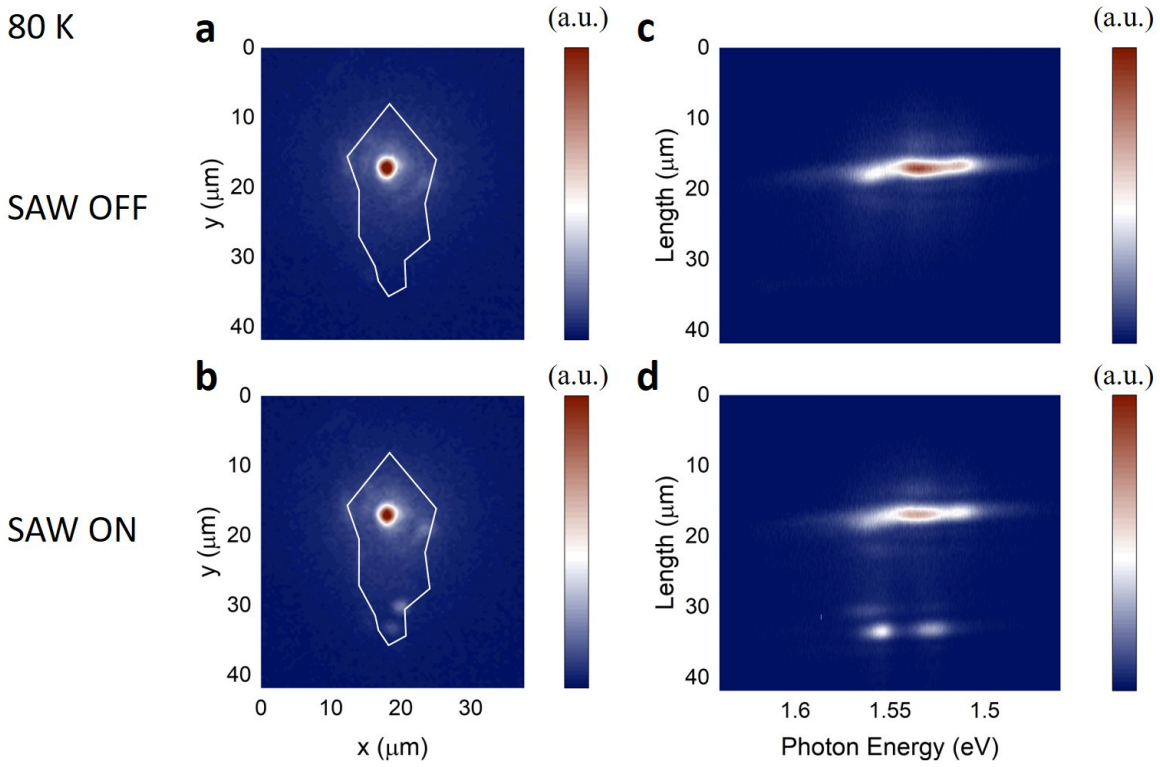

Supplementary Figure 7. Exciton transport at 120 K.

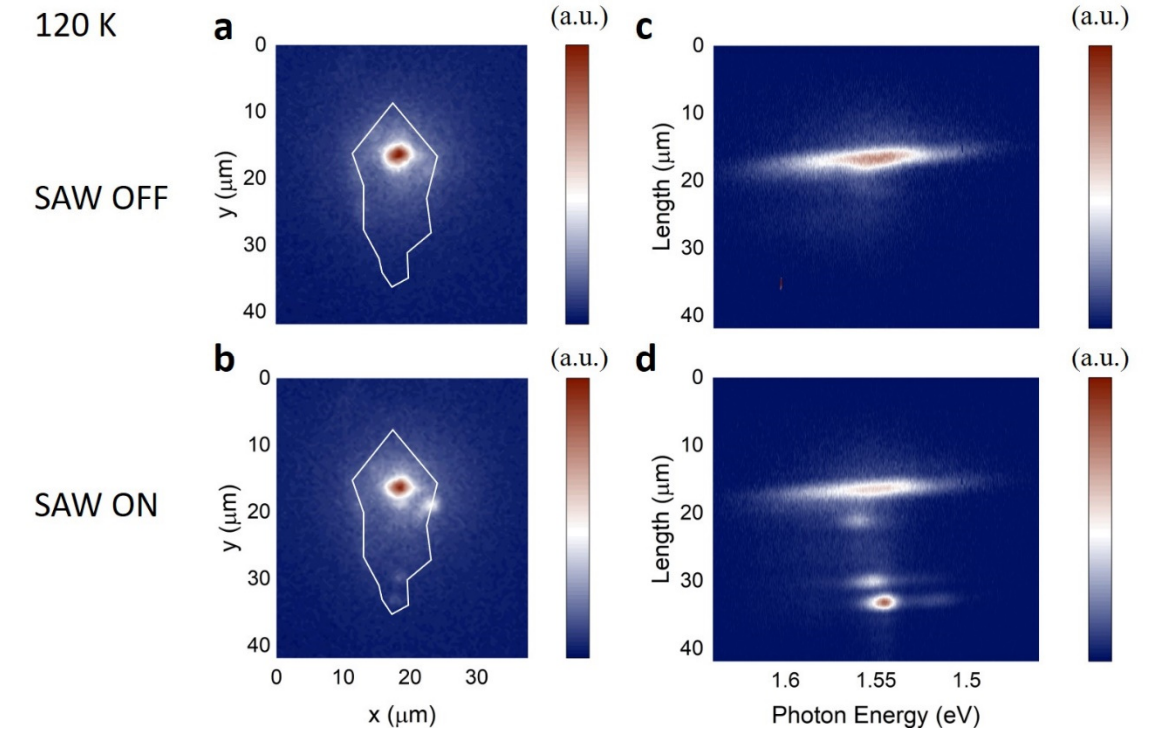

Supplementary Figure 8. Exciton transport at 290 K. The lower panels are zoomed in view of the dashed box. The exciton transport over ~2 μm can still be observed at room temperature owing to the strong SAW modulation.

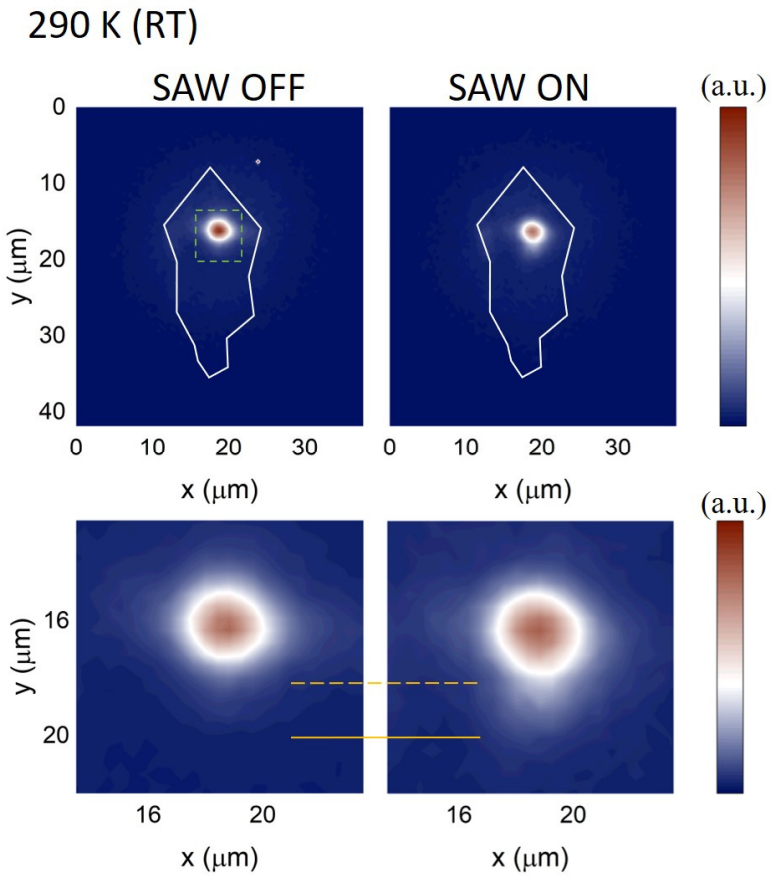

Supplementary Figure 9. Optical power-dependent measurement of exciton transport at 100 K with 6 mW SAW power. The portion of the transported exciton decreases with a higher optical pump. The high density of exciton could screen the piezoelectric field of SAW and reduce the acoustic modulation of the exciton energy.

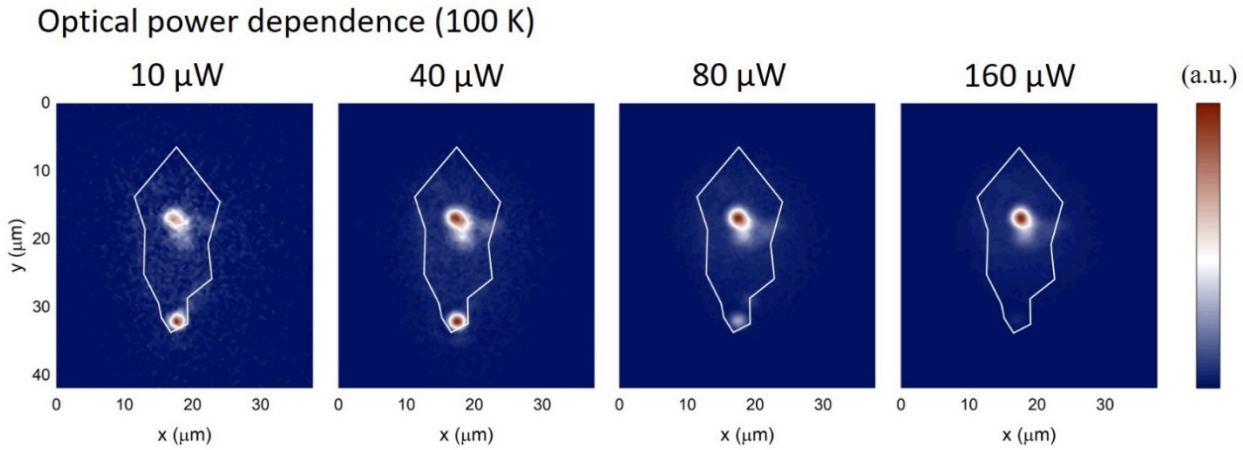

Supplementary Figure 10. The finite-element method (FEM) simulation of the SAW propagating on the $LiNbO_3$ substrate. (a) the magnified displacement of the SAW. (b), (c) the in-plane component of the piezoelectric field with and without ITO cladding. The ITO layer can strongly screen the in-plane field.

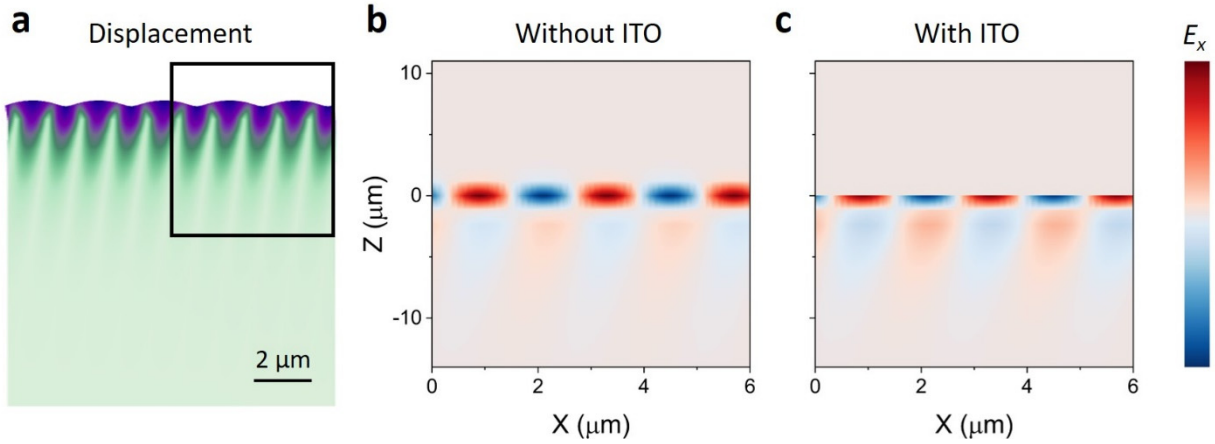

Supplementary Figure 11. RF calibration of the IDT acoustic transducers. (a) RF reflection coefficient S_{11} measurement of the IDT devices. We test the IDTs with varied number of periods N. Device with N=42 exhibits the best impedance matching according to the S_{11} measurements. (b) The vector analysis of the IDT resonance on a polar chart showing a strong acoustic resonance at 1.237 GHz with an on-resonance impedance 53.66 Ω+j3.77 Ω, closely matching the 50 Ω impedance of the RF source. (c) Equivalent circuit model of the IDT acoustic transducer for N=42 with component values of serial resistance R_s, shunt resistance R_l, capacitor C_e and admittance Y_a extracted from the data in (a) and (b).

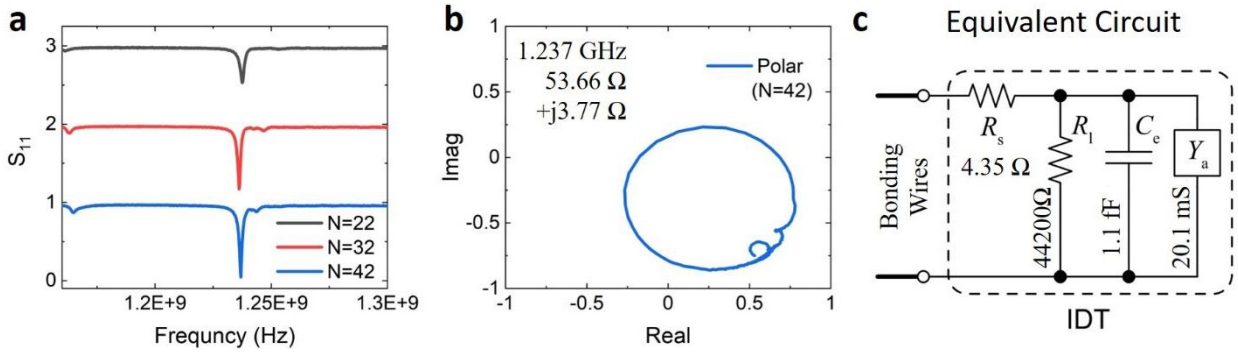

Supplementary Figure 12. The RF power ratio for different circuits components (Reflection, serial resistance R_s, shunt resistance R_l and admittance Y_a) calculated from the data in Fig.SI-11 (a) and (b). For N=42, the on-resonance conversion efficiency is 91% indicating a strong RF to acoustic wave conversion.

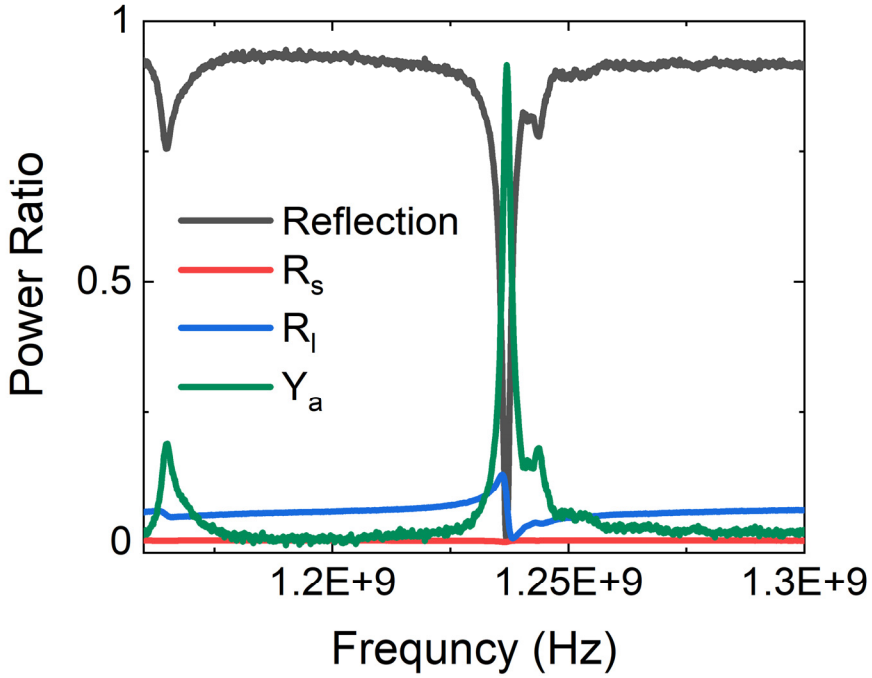

Supplementary Table 1. Simulated piezoelectric field at 10 nm above the $LiNbO_3$ substrate with the top ITO electrode. The ITO layer can provide an efficient screening of the in-plane field component for the SAW with different wavelengths.

Power density: 1 mW/μm

λ (μm)	0.6	1.2	1.8	2.4	3	3.6
f (GHz)	5.8568	2.9242	1.9497	1.4626	1.1703	0.97539
E_z (V/nm)	0.082	0.076	0.059	0.048	0.04	0.035
E_x (V/nm)	8.6×10^{-3}	4×10^{-3}	2.1×10^{-3}	1.3×10^{-3}	8.5×10^{-3}	6.1×10^{-3}

Reference:

1. Wilson, N. R. *et al.* Determination of band offsets, hybridization, and exciton binding in 2D semiconductor heterostructures. *Sci. Adv.* **3**, e1601832 (2017).

2. Nguyen, P. V. *et al.* Visualizing electrostatic gating effects in two-dimensional heterostructures. *Nature* **572**, 220–223 (2019).

3. Aslan, O. B., Deng, M., Brongersma, M. L. & Heinz, T. F. Strained bilayer WSe2 with reduced exciton-phonon coupling. *Phys. Rev. B* **101**, 115305 (2020).

4. Zomer, P. J., Guimarães, M. H. D., Brant, J. C., Tombros, N. & Van Wees, B. J. Fast pick up technique for high quality heterostructures of bilayer graphene and hexagonal boron nitride. *Appl. Phys. Lett.* **105**, 013101 (2014).

5. Purdie, D. G. *et al.* Cleaning interfaces in layered materials heterostructures. *Nat. Commun.* **9**, 5387 (2018).